8. E. Mazor, *Geochim. Cosmochim. Acta* **36**, 1321 (1972).
9. Stable isotope composition in groundwaters is controlled by the temperature and humidity prevailing during evaporation and during the condensation of precipitation, and by the large-scale atmospheric circulation patterns. It can later be altered by local evaporation, by mixing with melting ice or snow, and by water-rock interaction within the aquifer [M. Mazor, in *Chemical and Isotopic Groundwater Hydrology* (Dekker, New York, 1997), chap. 9].
10. M. Stute and P. Schlosser, in *Climate Change in Continental Isotopic Records*, P. K. Swart, K. C. Lohmann, J. McKenzie, S. Savin, Eds. (American Geophysical Union, Washington, DC, 1993), vol. 78, pp. 89–100.
11. L. Wyssling, *Hydrogeologische Erforschung des tiefliegenden Grundwasserstromes im oberen Glattal/ZH* (Report number 88.46, Office of Public Works (Baudirektion) of the Canton of Zürich, Department of Water Protection, Zürich, 1988).
12. J. N. Andrews, in *Isotopes of Noble Gases as Tracers in Environmental Studies* (International Atomic Energy Agency, Vienna, 1992), pp. 87–110; T. H. E. Heaton and J. C. Vogel, *J. Hydrol.* **50**, 201 (1981).
13. The processes responsible for this excess of atmospheric gases are not yet fully understood. Some experimental data indicate that the elemental ratios of the noble gas excesses correspond to the composition of unfractionated atmospheric air (*2*). A more sophisticated correction scheme, accounting for a fractionation of the excess air, has been proposed for cases when otherwise no consistent temperatures can be obtained from the different noble gases (*3*). In our study, the common correction with an excess of atmospheric composition yields coherent results, and no additional correction for fractionation is required.
14. E. Ingerson and F. J. Pearson, in *Recent Researches in the Fields of Atmosphere, Hydrosphere and Nuclear Geochemistry* (Nagoya University, Nagoya, Japan, 1964), pp. 263–283; J. C. Fontes and J. M. Garnier, *Water Resour. Res.* **15**, 399 (1979).
15. M. Stuiver and P. J. Reimer, *Radiocarbon* **35**, 215 (1993); E. Bard, B. Hamelin, R. G. Fairbanks, A. Zindler, *Nature* **345**, 405 (1990).
16. For each borehole *j*, the following three balance equations can be defined:

$$C^j_{k,s} = x^j \cdot C^j_{k,y} + (1 - x^j \cdot C^j_{k,o})$$

where x^j is the mixing ratio of the younger component and C^j_k is the concentration or activity (k = Cl^-, ^{39}Ar, or ^{14}C) of the sample (s), of the younger component (y), and of the older component (o). To allow the calculation of x^j, it was assumed that (i) the ^{14}C activity of the younger component is similar to the calculated initial activity of the sample; (ii) the dissolved inorganic carbon concentrations in the two components are comparable; (iii) the subsurface background ^{39}Ar equilibrium activity is constant in the whole aquifer (an assumption supported by constant ^{222}Rn and ^{37}Ar activities) and given by the lowest measured values at boreholes 1, 3 and 7 [~10% modern (Table 1)]; (iv) the older component contains no atmospheric ^{39}Ar; and (v) the ^{39}Ar activity and the Cl^- concentration of the younger component are the same in all samples.
17. M. Schüepp, in *Atlas der Schweiz*, E. Spiess, Ed. (Verlag der Eidgenössischen Landestopographie, Wabern-Bern, Switzerland, 1981), p. 11.
18. CLIMAP, *Science* **191**, 1131 (1976).
19. A. H. Bath, W. M. Edmunds, J. N. Andrews, in *Isotope Hydrology 1978* (International Atomic Energy Agency, Neuherberg, Vienna, 1979), vol. 2, pp. 545–568.
20. S. J. Johnsen, D. Dahl-Jensen, W. Dansgaard, N. Gundestrup, *Tellus* **47B**, 624 (1995).
21. B. Frenzel, in *Das Klima*, H. Oeschger, B. Messerli, M. Svilar, Eds. (Springer-Verlag, Berlin, 1980), pp. 45–63.
22. L. W. Gelhar, C. Welty, K. R. Rehfeldt, *Water Resour. Res.* **28**, 1955 (1992); A. Zuber, *J. Hydrol.* **86**, 45 (1986).
23. Y. Yurtsever and J. R. Gat, in *Stable Isotope Hydrology: Deuterium and Oxygen-18 in the Water Cycle*, J. R. Gat and R. Gonfiantini, Eds. (International Atomic Energy Agency, Vienna, 1981), pp. 103–142.
24. T. Sowers *et al.*, *Paleoceanography* **8**, 737 (1993).
25. The data from borehole 7 have been disregarded because the low $\delta^{18}O$ value and large excess air component of this sample (Table 1) may indicate that meltwater infiltrated during the short warmer climate period around 28 ky B.P. This might also account for the somewhat disturbed noble gas pattern, which results in a relatively large error in the calculated NGT at borehole 7.
26. U. Siegenthaler and H. Oeschger, *Nature* **285**, 314 (1980); M. Kullin and H. Schmassmann, in *Applied Isotope Hydrogeology, a Case Study in Northern Switzerland*, F. J. Pearson *et al.*, Eds. (Elsevier, Amsterdam, 1991), pp. 65–89.
27. W. Aeschbach-Hertig, F. Peeters, U. Beyerle, R. Kipfer, *Water Resour. Res.*, in preparation; noble gas solubilities are from R. F. Weiss, *Deep-Sea Res.* **17**, 721 (1970); *J. Chem. Eng. Data* **16**, 235 (1971); H. L. Clever, Ed., in *Krypton, Xenon and Radon—Gas Solubilities* (Pergamon, Oxford, 1979), pp. 1–226.
28. J. N. Andrews *et al.*, in *Isotope Hydrology 1983* (International Atomic Energy Agency, Vienna, 1984), pp. 535–576; H. H. Loosli, B. E. Lehmann, G. Däppen, in *Applied Isotope Hydrogeology, a Case Study in Northern Switzerland*, F. J. Pearson *et al.*, Eds. (Elsevier, Amsterdam, 1991), pp. 153–174.

29. This project was supported by the Swiss National Science Foundation (project no. 20-47060.96). We thank H. Baur, T. Graf, M. Möll, and S. Reese for assisting in the measurements; E. Hoehn for discussions; an anonymous reviewer for his or her comments; and D. Livingstone for linguistic improvements in the text.

3 June 1998; accepted 21 September 1998

Self-Organized Growth of Three-Dimensional Quantum-Dot Crystals with fcc-Like Stacking and a Tunable Lattice Constant

G. Springholz,* V. Holy, M. Pinczolits, G. Bauer

The self-organization of pyramidal PbSe islands that spontaneously form during strained-layer epitaxial growth of PbSe/$Pb_{1-x}Eu_xTe$ (x = 0.05 to 0.1) superlattices results in the formation of three-dimensional quantum-dot crystals. In these crystals, the dots are arranged in a trigonal lattice with a face-centered cubic (fcc)–like A-B-C-A-B-C vertical stacking sequence. The lattice constant of the dot crystal can be tuned continuously by changing the superlattice period. As shown by theoretical calculations, the elastic anisotropy in these artificial dot crystals acts in a manner similar to that of the directed chemical bonds of crystalline solids. The narrow size distribution and excellent control of the dot arrangement may be advantageous for optoelectronic device applications.

Semiconductor nanostructures have attracted tremendous interest in the past few years because of their special physical properties and their potential for applications in micro- and optoelectronic devices (*1*). In such nanostructures, the free carriers are confined to a small region of space by potential barriers, and if the size of this region is less than the electron wavelength, the electronic states become quantized at discrete energy levels. The ultimate limit of low dimensional structures is the quantum dot, in which the carriers are confined in all three directions. Therefore, a quantum dot can be thought of as an artificial atom. The fabrication of quantum dots presents a formidable challenge because the small dimensions required for quantum dots are at the limit of lithographic and semiconductor processing techniques and also because the dot interfaces must be kept defect-free in order to obtain the high-quality electronic properties that are required for device applications. As a consequence, many efforts have been made to develop alternative routes for the fabrication of quantum dots that are based on the principle of self-organization (*1–4*).

The spontaneous formation of three-dimensional (3D) islands in strained-layer heteroepitaxy has recently emerged as a new technique for the synthesis of self-assembled quantum dots (*3–6*). This technique is based on the fundamental morphological instability of strained surfaces, which is driven by the elastic relaxation of strain energy in the freestanding islands that spontaneously nucleate on the surface of a growing epitaxial layer after the completion of the wetting layer (*7*). In the early stage of growth, these islands are defect-free and fully coherent to the substrate (*8*). Therefore, quantum dots are obtained in situ without the interface problems that are associated with ex situ processing techniques. However, although single quantum dots exhibit extremely sharp, atomic-like luminescence properties (*5, 9*), the considerable inhomogenous line broadening in larger dot ensembles due to nonuniformities in the dot sizes has posed considerable limitations for device applications (*6, 10*).

G. Springholz, M. Pinczolits, G. Bauer, Institut für Halbleiterphysik, Johannes Kepler Universität Linz, 4040 Linz, Austria. V. Holy, Laboratory of Thin Films and Nanostructures, Faculty of Science, Masaryk University, Kotlarska 2, 611 37 Brno, Czech Republic.

*To whom correspondence should be addressed. E-mail: g.springholz@hlphys.uni-linz.ac.at

We studied the idea that the vertical elastic interaction of the strained 3D islands during the epitaxial growth of quantum-dot superlattices can lead to a lateral ordering and size homogenization of the dots (*11, 12*). Molecular beam epitaxy was used to fabricate PbSe quantum-dot superlattices, in which each dot layer is separated vertically by $Pb_{1-x}Eu_xTe$ spacer layers. For our materials, the ordering mechanism is so efficient that a nearly perfect hexagonal two-dimensional (2D) dot lattice was obtained within the growth plane after a few superlattice periods. Detailed high-resolution x-ray diffraction investigations revealed the existence of a dot correlation that is not parallel but is along crystallographical directions inclined by 39° to the growth direction. As a result, 3D quantum-dot crystals were formed with a fcc-like A-B-C-A-B-C stacking sequence. Theoretical calculations of the elastic interaction between the buried dots clearly showed that this special correlation, as well as the efficient lateral ordering, was directly connected to the high elastic anisotropy of the semiconductor compounds consisting of the group IV and VI elements of the periodic table (lead salt compounds). Because the symmetry of the dot arrangement is fixed by the elastic anisotropy, the lattice constant of the dot crystals can be tuned continuously over a range of several tens of nanometers just by changing the spacer layer thicknesses. This effect provides an opportunity for the tuning of optical and electronic properties.

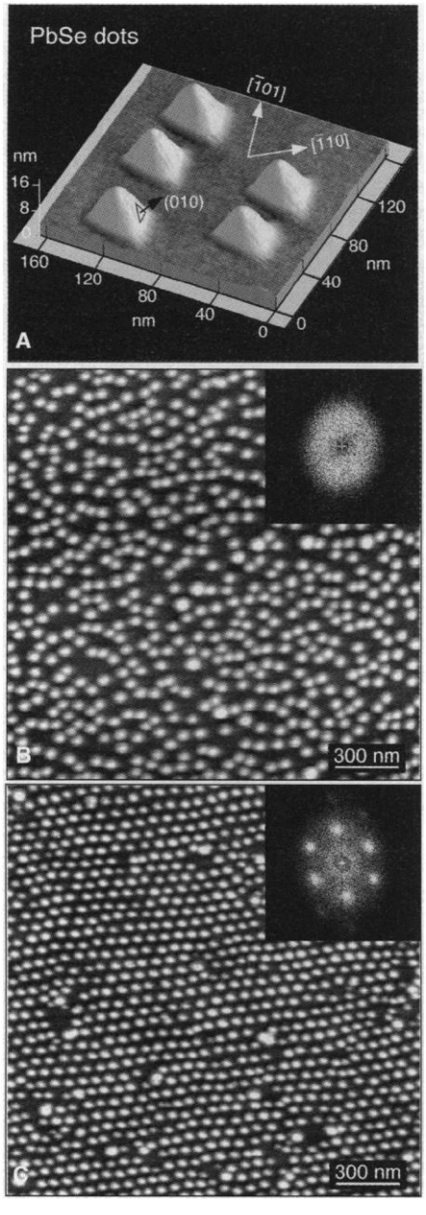

Fig. 1. (**A**) AFM image of pyramidal PbSe dots on PbTe (111) with {100} side facets. Large-scale AFM images of (**B**) a PbSe single layer on $Pb_{1-x}Eu_xTe$ and of (**C**) the last PbSe layer of a 60-period PbSe/$Pb_{1-x}Eu_xTe$ dot superlattice. The insets show the 2D power spectra of the AFM images.

Our superlattice samples were grown by molecular beam epitaxy on several-micrometer-thick PbTe buffer layers that were predeposited on (111)-oriented BaF_2 substrates. For the growth of the superlattice stacks, five PbSe monolayers were deposited, alternating with 30- to 70-nm-thick $Pb_{1-x}Eu_xTe$ spacer layers. The $Pb_{1-x}Eu_xTe$ composition (x = 5 to 10%) was adjusted so that the tensile stress in the PbSe layers was exactly compensated by the compressive stress in the spacer layers. In such strain-symmetrized superlattices, the number of bilayers can be increased infinitely without the formation of misfit dislocations. Because of the −5.5% lattice mismatch between PbSe and PbTe, strain-induced coherent PbSe islands are formed on the epitaxial surface when a critical coverage of 1.5 monolayers is exceeded (*13*). These islands have a pyramidal shape with a triangular base and very steep side facets (Fig. 1A). The side facets are inclined by 54.7° with respect to the (111) growth plane and are aligned parallel to the threefold ⟨$\bar{1}$10⟩ directions. Thus, the facets are formed by the three lowest free-energy {100} surface planes.

In situ high-energy electron diffraction and ex situ atomic force microscopy (AFM) studies showed that, during the growth of the dot superlattices, an identical island formation behavior occurs during the deposition of each PbSe layer and that a complete replanarization of the surface occurs during the growth of the spacer layers. An AFM image of the last PbSe dot layer of a 60-period superlattice stack is shown in Fig. 1C, in comparison with that of a single PbSe layer (Fig. 1B). In the single PbSe layer, the dots are distributed randomly with an average spacing of ~61 nm, whereas in the superlattices with an increasing number of periods N, increasingly larger regions of perfect hexagonally ordered dots are formed. When $N > 30$, the nearly perfect hexagonal arrangement is disrupted only by point defects (missing dots or dots at interstitial positions) or, occasionally, by additionally inserted dot rows ("dislocations") (Fig. 1C). The improvement of the lateral order can be characterized by the analysis of the 2D power spectrum of the AFM images (Fig. 1, B and C, insets). For the single layer, the power spectrum exhibits only a broad and diffuse ring, whereas six side maxima appear after only a few superlattice periods, corresponding to the onset of hexagonal ordering. For larger N, these six maxima rapidly sharpen, and the diffuse background is drastically reduced. For N = 60,

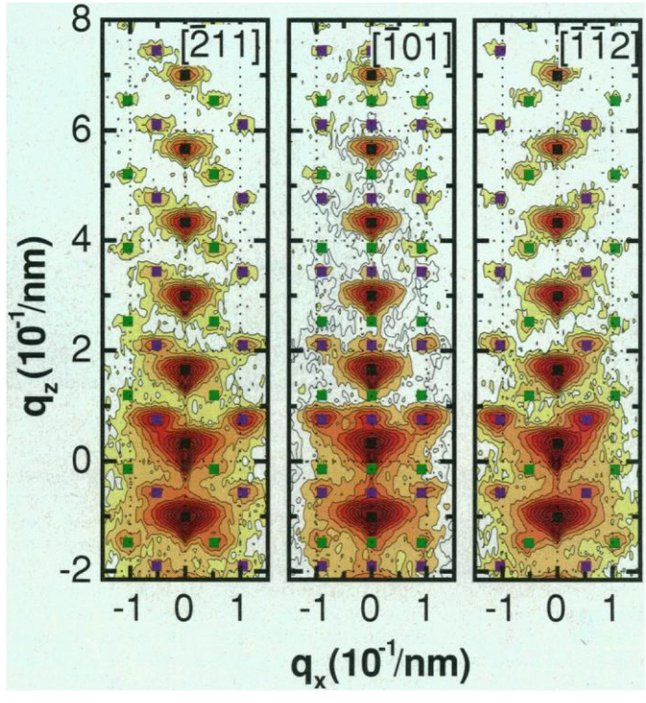

Fig. 2. RSMs of diffracted intensity around the (222) reflection of a 60-period PbSe/$Pb_{1-x}Eu_xTe$ dot superlattice with D_{SL} = 46 nm measured in three different azimuth directions [$\bar{2}$11], [$\bar{1}$01], and [$\bar{1}\bar{1}$2]. Blue, black, and green squares are the intensity maxima according to the reciprocal dot lattice as defined in the text, and as shown schematically in Fig. 3A with the identical color coding of the squares.

the ratio of the peak width and the peak position in the power spectrum is ~1:8, which indicates that the perfectly ordered regions contain >60 single PbSe dots. In addition, the size distribution narrows to ±7%.

To obtain information on the vertical stacking of the dots, we used coplanar high-resolution x-ray diffraction to record the diffracted intensity as a function of the various diffraction angles. The measured angular intensity distribution was transformed into reciprocal space coordinates, taking into account the scattering geometry. Reciprocal space maps (RSMs) (Fig. 2) were measured in three different azimuth directions ([$\bar{2}$11], [$\bar{1}$01], and [$\bar{1}\bar{1}$2]) within the (111) surface. In the RSMs, q_z is parallel to the [111] surface normal, and the origin coincides with the (222) reflection of the PbTe buffer layer. In contrast to the rather diffuse x-ray scattering that was observed for disordered dot superlattices (*14*), a large number of satellite peaks appear in the RSMs not only along q_z but also in the q_x directions parallel to the surface.

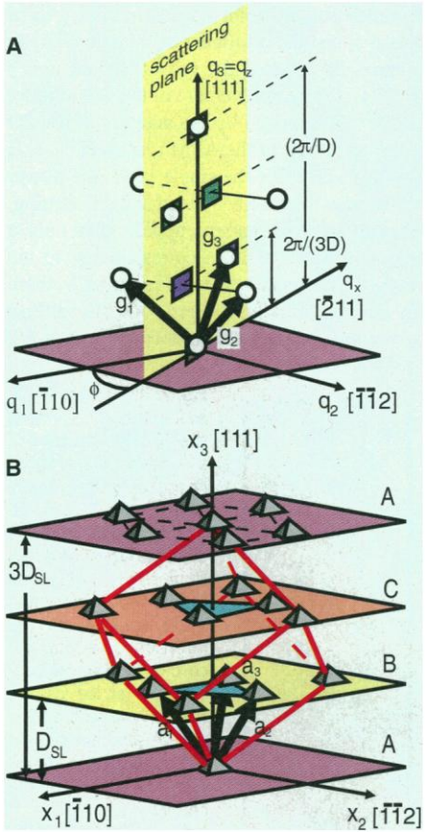

Fig. 3. Illustration of the (**A**) reciprocal and (**B**) real-space lattices that were formed by the self-organized PbSe quantum dots. In (A), the points of the reciprocal lattice are represented by red spheres, and their projections to the scattering plane are represented by squares. In (B), the PbSe dots are represented by gray pyramids, and the vertical stacking sequence is denoted by A, B, and C. As indicated by the form of the red lines, the elementary unit cell is nearly cubic.

The appearance of these peaks proves that the dot positions are highly correlated both laterally and vertically; that is, the dots create a periodic lattice in all three directions. For the [$\bar{1}$01] azimuth, the intensity distribution is symmetric with respect to the surface normal q_z. However, for the [$\bar{2}$11] and [$\bar{1}\bar{1}$2] azimuths, the two maps are mirror-symmetric with respect to each other. This observation indicates a reduced threefold symmetry of the [111] growth axis as opposed to the sixfold symmetry on the surface observed by AFM, with the existence of three mirror planes that are perpendicular to the {01$\bar{1}$} planes. Therefore, the point symmetry group of the dot lattice is 3*m*, which belongs to the trigonal syngony.

For normal 2D semiconductor superlattices, the spacing of the intensity maxima along the q_z growth direction is determined only by the superlattice period D_{SL}, which is the sum of the $Pb_{1-x}Eu_xTe$ and PbSe layer thicknesses. However, in the RSMs of our dot superlattices, two additional maxima appear along the q_z growth direction between the regular superlattice satellite peaks (see the [$\bar{1}$01] azimuth in Fig. 2). Thus, the periodicity of the dot lattice along [111] is three times D_{SL}. These observations (the tripling of the vertical periodicity and the reduced overall symmetry) indicate that, in contrast to all dot superlattices studied so far (*12, 14, 15*), the correlation of the PbSe dots in successive layers is not parallel but inclined to the growth direction.

To deduce the 3D arrangement of the PbSe dots from the RSMs, we had to account for the actual scattering geometry. Because our x-ray primary beam had a small divergence within the scattering plane but a 1° divergence perpendicular to it, the lateral intensity maxima in the RSMs were produced by orthogonal projections of the reciprocal lattice points within $q_y = \pm 0.3$ nm^{-1} onto the scattering plane (Fig. 3A, squares). By the three reciprocal basic vectors $\mathbf{g}_1$, $\mathbf{g}_2$, and $\mathbf{g}_3$

$$\begin{pmatrix}\mathbf{g}_1\\ \mathbf{g}_2\\ \mathbf{g}_3\end{pmatrix} = \begin{pmatrix}\sqrt{3}h/2 & -h/2 & H/3\\ 0 & h & H/3\\ -\sqrt{3}h/2 & -h/2 & H/3\end{pmatrix}$$

a set of reciprocal lattice points was defined (Fig. 3A, red spheres) (h and H define the coordinates of the reciprocal basic vectors $\mathbf{g}_i$ in the coordinate system shown in Fig. 3A). The values of h and H can be determined directly from the lateral and vertical distance of the RSM maxima, which yields $h = 0.105$ nm^{-1} and $H = 0.133$ nm^{-1} with an error of ±0.004 nm^{-1}. As indicated by the colored squares in Fig. 2, the reciprocal lattice points defined in this manner coincide very well with the intensity maxima that were observed in the measured RSMs.

From the real-space transformation of the reciprocal basic vectors $\mathbf{g}$ (transposition and inversion of the reciprocal space basic vectors $\mathbf{g}_i$), the coordinates of the basic vectors $\mathbf{a}_i$ in real space are obtained as

$$\begin{pmatrix}\mathbf{a}_1\\ \mathbf{a}_2\\ \mathbf{a}_3\end{pmatrix} = \begin{pmatrix}\sqrt{3}b/2 & -b/2 & D\\ 0 & b & D\\ -\sqrt{3}b/2 & -b/2 & D\end{pmatrix}$$

with $b = 39 \pm 2$ nm and $D = 47 \pm 2$ nm (b and D define the coordinates of the real-space basic vectors $\mathbf{a}_i$ in the coordinate system shown in Fig. 3B). It turns out that D is equal to the preset superlattice period D_{SL}. On a given interface, the dots thus create a regular hexagonal grid (Fig. 3B) with a distance L between neighboring dots of $L \equiv b \times \sqrt{3} = 67 \pm 3$ nm. This distance is equal to the value that was determined by AFM. In the [111] growth direction, three different interface planes can be distinguished, which are laterally displaced by b with respect to each other, resulting in an A-B-C-A-

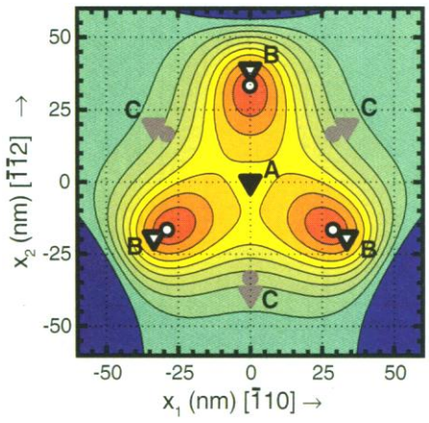

Fig. 4. Distribution of the elastic energy density Σ on the (111) $Pb_{1-x}Eu_xTe$ surface that was calculated for a PbSe force nucleus in the depth of 47 nm. At the minima of Σ (dark orange), the misfit strain is locally reduced by ~2%. The regions with increased Σ are blue. The observed PbSe dot positions at interfaces A, B, and C are denoted by black, gray, and white triangles, respectively. The gray and white circles denote the dot positions in a cubic fcc lattice.

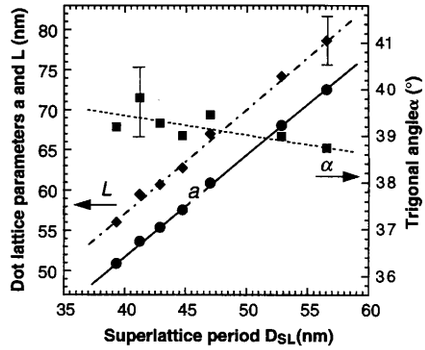

Fig. 5. Experimentally determined in-plane dot-dot distance L (diamonds), dot crystal lattice constant a (circles), and trigonal angle α (squares) for several PbSe/$Pb_{1-x}Eu_xTe$ dot superlattices that are plotted as a function of the superlattice period D_{SL}.

B-C stacking sequence like that of the (111) planes in fcc lattices. This sequence is the origin of the tripling of the periodicity along the growth direction. For a perfect fcc lattice, the D/L ratio between the vertical separation of the dot planes and the in-plane dot distance should be equal to 0.866. However, for our sample, this ratio equals 0.704. Thus, the trigonal dot lattice can be thought of as a fcc lattice that is compressed by 18% along the body diagonal. This yields a trigonal angle α of 39.5° between the a_i and the [111] directions instead of 35.26° for the cubic case.

To obtain such a stacking sequence solely by epitaxial growth, the nucleation of dots must occur along the $\mathbf{a}_1$, $\mathbf{a}_2$, and $\mathbf{a}_3$ directions with respect to the dots in the previous layer, in contrast to the preferred nucleation along the growth direction observed for other material systems (*12, 14, 15*). This behavior can be induced only by a nonuniform in-plane strain distribution on the surface that is produced by the lattice distortions around the buried dots, with an enhanced dot nucleation probability at surface positions of lower elastic energy density Σ. For elastically isotropic materials, however, the absolute minimum of Σ occurs exactly above the previous dots (*11, 12*); that is, the dots in a multilayer should be aligned vertically. To resolve this issue, we performed elastic strain field calculations that accounted for the elastic anisotropy of the lattice. To simplify these calculations, we replaced the actual dot with an infinitely small "force nucleus" and neglected the surface relaxation of the internal stresses. The in-plane strain on the surface was then calculated with a Fourier method to solve the Navier equation (*16*). As shown in Fig. 4, the calculated elastic energy density Σ on a (111) $Pb_{1-x}Eu_xTe$ surface with a PbSe dot at 47 nm below the surface exhibits a $3m$ point symmetry with three pronounced energy minima that are displaced laterally from the subsurface force nucleus. These minima coincide almost exactly with the experimentally observed dot positions (Fig. 4). In addition, a saddle point of Σ occurs in the center, above the buried dot, which indicates that this point is not favorable for the growth of a subsequent dot.

The directions of the Σ minima are determined only by the elastic anisotropy of the matrix material. Therefore, the symmetry of the dot arrangement should be essentially independent of the spacer thickness. To verify this conclusion, we fabricated a series of PbSe/ $Pb_{1-x}Eu_xTe$ dot superlattices with spacer thicknesses that varied from 35 to 60 nm. The lateral and vertical separation L and D, respectively, of the dots in each sample was determined from RSMs. We found that, for D_{SL} varying almost by a factor of 2, the trigonal angle α of the dot lattice indeed remains nearly constant (Fig. 5). Moreover, the lateral dot distance L and the dot crystal lattice constant a change linearly with spacer thickness (Fig. 5). Thus, the PbSe dot samples represent macroscopic crystals with a continuously tunable lattice constant. Furthermore, for a constant-deposited PbSe thickness, with varying L (varying dot density), the average dot volume changes with D_{SL} as well.

Because of their atomic-like density of states, semiconductor quantum dots offer many advantages for optoelectronic devices. For such applications, however, a high density of dots and a narrow size distribution are of crucial importance (*1, 6, 10*). The excellent control of absolute size, as well as of lateral distance that can be achieved by the growth of quantum-dot superlattices, thus allows great improvements for the precise tuning of the optical and electronic properties of self-assembled quantum dots. This opens promising perspectives for their applications in semiconductor diode lasers (*1, 6, 10*), intersubband infrared detectors (*17*), and microcavity devices (*18*).

References and Notes

1. A. P. Alivisatos, *Science* **271**, 933 (1996), and references therein.
2. C. B. Murray, C. R. Kagan, M. G. Bawendi, *ibid.* **270**, 1335 (1995).
3. D. Leonhard *et al.*, *Appl. Phys. Lett.* **63**, 3203 (1993); J. M. Moison *et al.*, *ibid.* **64**, 196 (1994).
4. R. Nötzel, J. Temmyo, T. Tamamura, *Nature* **369**, 131 (1994).
5. R. Leon P. M. Petroff, D. Leonard, S. Fafard, *Science* **267**, 1966 (1995).
6. S. Fafard *et al.*, *ibid.* **274**, 1350 (1996).
7. R. J. Asaro and W. A. Tiller, *Metall. Trans.* **3**, 1789 (1972); D. J. Srolovitz, *Acta Metall.* **37**, 621 (1989); C. Ratsch and A. Zangwill, *Surf. Sci.* **293**, 123 (1993).
8. D. J. Eaglesham and M. Cerullo, *Phys. Rev. Lett.* **64**, 1943 (1990); S. Guha, A. Madhukar, K. C. Rajkumar, *Appl. Phys. Lett.* **57**, 2110 (1990).
9. J. Y. Marzin *et al.*, *Phys. Rev. Lett.* **73**, 716 (1994); M. Grundman *et al.*, *ibid.* **74**, 4043 (1995); L. Landin, M. S. Miller, M.-E. Pistol, C. E. Pryor, L. Samuelson, *Science* **280**, 262 (1998).
10. N. Kirstaedter *et al.*, *Electron. Lett.* **30**, 1416 (1994); V. Y. Shchukin *et al.*, *Phys. Rev. B* **57**, 12262 (1998).
11. J. Tersoff, C. Teichert, M. G. Lagally, *Phys. Rev. Lett.* **76**, 1675 (1996).
12. Q. Xie, A. Madhukar, P. Chen, N. Kobayashi, *ibid.* **75**, 2542 (1995).
13. M. Pinczolits, G. Springholz, G. Bauer, *Appl. Phys. Lett.* **73**, 250 (1998).
14. A. Darhuber *et al.*, *Phys. Rev. B* **55**, 15652 (1997).
15. G. S. Solomon, J. A. Trezza, A. F. Marshall, J. S. Harris, *Phys. Rev. Lett.* **76**, 952 (1996).
16. R. A. Masumura and G. Sines, *J. Appl. Phys.* **41**, 3930 (1970); J. W. Flocken and J. R. Hardy, *Phys. Rev. B* **1**, 2447 (1970).
17. S. Sauvage *et al.*, *Appl. Phys. Lett.* **71**, 2785 (1997).
18. J. M. Gérard *et al.*, *Phys. Rev. Lett.* **81**, 1110 (1998).

19. This work was supported by the Austrian Science Fund (grant 11557), the Jubiläumfonds of the Austrian National Bank (grant 6690), the Gesellschaft für Mikroelektronik Austria, the grant agency of the Czech Republic (grant 202/97/0003), and the Ministry of Education of the Czech Republic (grant VS96102).

27 July 1998; accepted 15 September 1998

Rapid Identification of Subtype-Selective Agonists of the Somatostatin Receptor Through Combinatorial Chemistry

Susan P. Rohrer,* Elizabeth T. Birzin, Ralph T. Mosley, Scott C. Berk, Steven M. Hutchins, Dong-Ming Shen, Yusheng Xiong, Edward C. Hayes, Rupa M. Parmar, Forrest Foor, Sudha W. Mitra, Sylvia J. Degrado, Min Shu, John M. Klopp, Sheng-Jian Cai, Allan Blake, Wanda W. S. Chan, Alex Pasternak, Lihu Yang, Arthur A. Patchett, Roy G. Smith, Kevin T. Chapman, James M. Schaeffer

Nonpeptide agonists of each of the five somatostatin receptors were identified in combinatorial libraries constructed on the basis of molecular modeling of known peptide agonists. In vitro experiments using these selective compounds demonstrated the role of the somatostatin subtype-2 receptor in inhibition of glucagon release from mouse pancreatic alpha cells and the somatostatin subtype-5 receptor as a mediator of insulin secretion from pancreatic beta cells. Both receptors regulated growth hormone release from the rat anterior pituitary gland. The availability of high-affinity, subtype-selective agonists for each of the somatostatin receptors provides a direct approach to defining their physiological functions.

Somatostatin is distributed throughout the endocrine system and has multiple physiological functions including inhibition of secretion of growth hormone (*1*), glucagon (*2*), insulin (*3*), gastrin, and other hormones secreted by the pituitary and gastrointestinal tract (*4*). It also acts as a neuromodulatory peptide in the central nervous system (*5*) and has been im-